Model-based Iterative Reconstruction for Neutron Laminography

S. V. Venkatakrishnan*, Ercan Cakmak†, Hassina Billheux§, Philip Bingham*, Richard K. Archibald‡
* Imaging, Signals and Machine Learning Group, Oak Ridge National Lab, Oak Ridge, TN 37831
† Material Science and Technology Group, Oak Ridge National Lab, Oak Ridge, TN 37831
‡ Computer Science and Applied Mathematics Group, Oak Ridge National Lab, Oak Ridge, TN 37831
§ Neutron Sciences Directorate, Oak Ridge National Lab, Oak Ridge, TN 37831

***Abstract*—Neutron-based parallel-beam laminography is an important 3D characterization tool because it can image thick specimens with unique shapes and provides a complimentary contrast to X-rays for several elements relevant to the material sciences and biology. However, the inversion of neutron laminography data is complicated because of the non-traditional geometry of the set-up, the presence of noise and the occurrence of gamma hits on the detector during the course of an experiment.**

In this paper, we present a model-based/regularized-inversion reconstruction algorithm for neutron laminography. We introduce a new forward-model/data fitting term and combine it with a flexible regularizer function to formulate the reconstruction as minimizing a cost-function. We then present a novel optimization algorithm that is based on combining a majorization-minimization technique with a first-order method that is amenable to simple parallelization on multi-core architectures. Using simulated and experimental data, we demonstrate that it is possible to acquire high quality reconstructions compared to the typically used filtered-back projection algorithm and algebraic reconstruction techniques.

I. Introduction

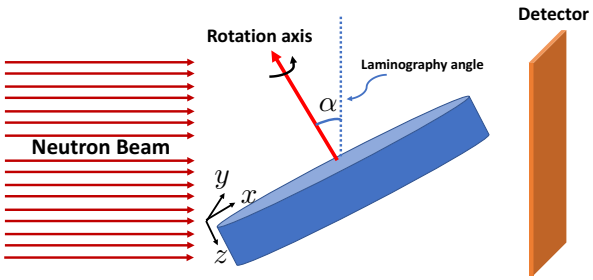

Fig. 1. Illustration of the set-up used for neutron laminography. The sample is tilted by an angle α, rotated and imaged, allowing for thin lamellar samples to be measured without heavily attenuating the beam. When $\alpha = 0$, this set-up corresponds to conventional parallel-beam tomography.

Laminography refers to a set of techniques that have been developed to reconstruct samples which have large lateral dimensions which make them difficult to scan using conventional tomography geometries [1]. Along with tomosynthesis [2] and limited-angle tomography [3], laminography represents a variant of conventional computed tomography (CT) in which the source, object and detector are oriented in a manner such that sufficient measurements of the projections of the object can be made and used to reconstruct the sample reliably. Laminography has been demonstrated to be useful in several applications including defect detection in semiconductor wafers [4], characterizing historic artifacts [5], and reconstructing polymer lamellar samples [6]. In summary, with the growing use of tomographic techniques to characterize samples with varied shapes for emerging applications such as additive manufacturing, laminography is a vital tool for characterizing samples in 3D.

This manuscript has been authored by UT-Battelle, LLC, under Contract No. DE-AC05-00OR22725 with the U.S. Department of Energy. The United States Government and the publisher, by accepting the article for publication, acknowledges that the United States Government retains a non-exclusive, paid-up, irrevocable, world-wide license to publish or reproduce the published form of this manuscript, or allow others to do so, for United States Government purposes. DOE will provide public access to these results of federally sponsored research in accordance with the DOE Public Access Plan (http://energy.gov/downloads/doe-public-access-plan).

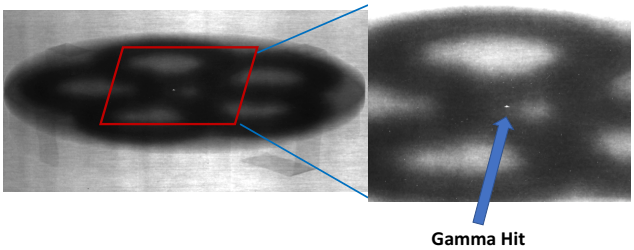

Fig. 2. Illustration of a single radiograph from a neutron laminography experiment of an additively manufactured thin cylindrical metallic part. Notice that in the zoomed in section there is a set of pixels that are bright (contrast adjusted for emphasis) caused by gamma rays hits on the detector. Typically, there are several such hits at various locations and at different images in the data set.

As with conventional CT, laminography techniques have been developed for cone-beam geometries using table-top X-rays systems [7] and for parallel-beam geometries using synchrotron based X-rays [8] and neutron sources [9]. In this paper, we focus on algorithms for parallel-beam laminography in which a sample is tilted, rotated, imaged (see Fig. 1) and then reconstructed. Neutron-based parallel-beam laminography [5], [9], typically carried out at high-flux research reactors or pulsed-neutron facilities, is an important 3D characterization tool because it can image thick specimens with unique shapes and made of "high-Z" (atomic number) materials. In particular, since neutron cross-section is not correlated with the atomic number of an element like for X-rays, neutrons can penetrate materials made of high-Z elements more easily than X-rays. However, the inversion of neutron laminography data is complicated because of the non-traditional geometry of the set-up, the presence of noise and the occurrence of

gamma hits on the detector (see Fig. 2) during the course of an experiment.

The most widely used algorithms for parallel-beam neutron laminography are based on pre-processing the data to deal with the gamma hits followed by the application of a variant of the filtered back-projection algorithm [10], [11] or an algebraic reconstruction technique [12]. However, due to the geometry of the set-up, there are typically "missing cones" of information in Fourier-space [10], resulting in noisy reconstructions with artifacts and a loss of resolution due to the pre-processing. The reconstructions may also be affected by streaks due to the presence of the gamma hits if these are not detected and filtered-out by the pre-processing steps. Furthermore, algebraic reconstruction techniques like SIRT [13] do not have a well defined convergence behavior and may result in increased noise as the number of iterations increases. In summary, while the conventional approaches for parallel-beam laminography provide a reasonable reconstruction there are still several challenges in being able to obtain high-quality reconstructions from typical data sets.

Model-based inversion techniques [14], which involve formulating and minimizing a cost-function that balances a data fitting term (derived from a forward model) and a regularizer (derived from a prior model) have been shown to dramatically improve reconstruction quality for several limited-angle [15], [16], sparse-view [17], [18] and low-dose tomography applications [19]. Recently, such techniques have been developed for cone-beam X-ray laminography [20], [21], showing improvements in image quality over the standard approaches. However, these approaches do not account for the occurrence of gamma hits and the Poisson-like characteristics of the noise. Furthermore, these approaches are strongly coupled to a the total-variation regularizer which is best suited to samples with "discrete" regions with sharp edges.

In this paper, we present a model-based reconstruction algorithm for parallel-beam neutron laminography. First, we design a new forward model/data-fitting term that combines a projection matrix that models the complex geometry of the system, a data-dependent weighting term for modeling the noise and a penalty term based on a Huber-like function [22] that is robust to outliers. We then present a novel optimization algorithm that is based on combining a majorization-minimization [15]–[18], [23], [24] technique with a first-order method inspired by the optimized-gradient method [25] that is amenable to simple parallelization on multi-core architectures. Using simulated and experimental data, we demonstrate that it is possible to acquire high quality reconstructions compared to the typically used filtered-back projection algorithm and algebraic reconstruction techniques even without pre-processing the data sets to filter-out the gamma hits.

II. Formulating the Cost Function

Neutron laminography is a parallel-beam transmission modality in which we estimate the attenuation coefficients of the sample from a collection of measured transmission images that are corrupted by noise as well as gamma-hits. In order to reconstruct the attenuation coefficients associated with the sample, we use the MBIR [19] framework. The reconstruction

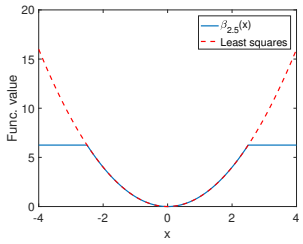

Fig. 3. Illustration of the Talwar function β_T for $T = 2.5$. The red dashed line shows the typically used least-squares penalty in several algorithms.

is formulated as a minimization problem,

$$\hat{f} = \underset{f}{\operatorname{argmin}} \{l(g; f) + s(f)\} \tag{1}$$

where g is the vector of log-normalized measurements, f is the vector containing all the attenuation coefficients, $l(;)$ is a data fidelity enforcing function and $s(.)$ is a function that enforces regularity in f. We utilize a data-fidelity term that is designed to handle outliers [16], [17], [22], [26] of the form

$$l(g; f) = \frac{1}{2} \sum_{i=1}^{M} \beta_T((g_i - [Af]_i)\sqrt{W_{ii}}) \tag{2}$$

where A is a forward projection matrix, W is a diagonal matrix with entries set to be the inverse variance of the noise in g_i,

$$\beta_T(x) = \begin{cases} x^2 & |x| < T \\ T^2 & |x| \geq T \end{cases}$$

is a generalization of the Huber function [27] (also called the Talwar function [28], [29]) (see Fig. 3) and T is the outlier threshold. The particular form of β_T function is a more accurate model for data with outliers compared to the widely used quadratic penalty [30]. The entries of W are set such that $W_{ii} = \lambda_i$, where λ_i is the raw un-normalized measurement [30]. We design A to model the laminography geometry of our set-up by using the ASTRA tool-box [31], [32] that can utilize multiple GPUs [33], [34] to accelerate the application of this matrix.

For $s(f)$, we choose the negative log of q-generalized Markov-random field (qGGMRF) probability density function [35]. It is given by

$$\begin{aligned} s(f) &= \sum_{\{j,k\} \in \mathcal{N}} w_{jk} \rho(f_j - f_k) \\ \rho(f_j - f_k) &= \frac{\left| \frac{f_j - f_k}{\sigma_f} \right|^2}{c + \left| \frac{f_j - f_k}{\sigma_f} \right|^{2-p}} \end{aligned}$$

$\mathcal{N}$ is the set of pairs of neighboring voxels (e.g. a 26 point neighborhood), $1 \leq p \leq 2$, c and σ_f are qGGMRF parameters. The weights w_{jk} are inversely proportional to the distance between voxels j and k, normalized to 1. This model provides a greater degree of flexibility in the range of reconstructions compared to an algorithm specifically designed for a total-variation regularizer [36] that may force the reconstructions to appear "waxy" [14]. In particular, when $p = 1$ we get a behavior similar to a total-variation model and when $p = 2$

the regularizer is a quadratic function allowing for smoother reconstructions.

Combining the data fidelity model (2) with the image model (3) the MBIR cost function is

$$c(f) = \frac{1}{2}\sum_{i=1}^{M} \beta_T \left((g_i - [Af]_i)\sqrt{W_{ii}} \right) + s(f) \qquad (3)$$

Thus, the reconstruction is obtained by

$$\hat{f} \leftarrow \underset{f}{\operatorname{argmin}}\, c(f)$$

This function in non-convex and non-differentiable and hence we will use a majorization strategy to find a solution.

III. Optimization Algorithm

In this section we outline the majorize-minimize (MM) optimization strategy from [26] for finding a minima of the MBIR cost function (3). The MM optimization approach [23], [24] is based on the repeated construction and decrease in value of a differentiable majorizer to the original cost function. The function $q(.; z')$ is a majorizer for the function $t(.)$ at the point z' if the following two conditions hold [14]

$$\begin{aligned} q(z; z') &\geq t(z) \\ q(z'; z') &= t(z'). \end{aligned} \qquad (4)$$

If $Q(.; f')$ is a majorizer to $c(.)$ at the point f', our algorithm consists of repeatedly constructing Q and updating the volume to obtain a desirable solution.

A. Construction of the Majorizer

It was shown in [16], that

$$Q_T(x; x') = \begin{cases} x^2 & |x'| < T \\ T^2 & |x'| \geq T \end{cases}$$

is a majorizer to β_T ((3)) at x'. Defining $e_i(f) = g_i - [Af]_i$ and using the composition property of majorizing functions [16]

$$\tilde{Q}(f; f') = \frac{1}{2}\sum_{i=1}^{M} Q_T \left(e_i(f)\sqrt{W_{ii}}; e_i(f')\sqrt{W_{ii}} \right) + s(f) \qquad (5)$$

is a majorizer to the original cost (3). This can be re-written in a simpler form by defining

$$W'_{ii} = \begin{cases} W_{ii} & |e_i(f')\sqrt{W_{ii}}| < T \\ 0 & |e_i(f')\sqrt{W_{ii}}| \geq T \end{cases} \qquad (6)$$

where the entries W' essentially ignore measurements classified as an outlier based on the current values of the scaled fitting error. Ignoring constants, (5) can be re-written as

$$Q(f; f') = \frac{1}{2}\|g - Af\|^2_{W'} + s(f). \qquad (7)$$

B. Updating the Voxels

Instead of using a coordinate descent strategy to decrease a similar function as in [16], [18], [26], we propose a parallel update strategy in-order to make use of the fast and parallel projection (and back-projection) operations for the laminography geometry. To update the volume based on this surrogate function (7) we adopt a modified version of the optimized gradient method (OGM) of Kim and Fessler [25]. A straight forward method to implement this algorithm would be to run a few iterations of OGM to decrease the surrogate cost for Q, then use this new value as the the updated volume and iterate the process. This method would involve re-setting the momentum factors for each set of "inner" iterations involving the decrease of Q. Instead, we adopt a different approach that involves only one iteration of the OGM method, but carry forward the momentum factors from the previous iteration. Specifically, at the k^{th} iteration we apply the following steps,

$$\begin{aligned} h^{(k+1)} &\leftarrow f^{(k)} - \frac{1}{L}\nabla Q(f; f^{(k)})|_{f=f^{(k)}} \\ t^{(k+1)} &\leftarrow \frac{1 + \sqrt{1 + 4(t^{(k)})^2}}{2} \\ f^{(k+1)} &\leftarrow h^{(k+1)} + \frac{t^{(k)} - 1}{t^{(k+1)}}(h^{(k+1)} - h^{(k)}) + \\ &\qquad \frac{t^{(k)}}{t^{(k+1)}}(h^{(k+1)} - f^{(k)}) \end{aligned} \qquad (8)$$

where L is set so that $L = \max\{\text{diag}(A^T W A) + \text{diag}(\nabla^2 s(0))\} \geq \max\{\text{diag}(A^T W^{(k)} A) + \text{diag}(\nabla^2 s(f^{(k)}))\}$, an upper-bound on the Lipschitz constant of the gradient of the surrogate function at any given iteration and $t^{(0)} = 1$. The gradient of Q w.r.t f is

$$\nabla Q(f; f') = -A^T W'(g - Af) + \nabla s(f) \qquad (9)$$

Hence the overall updates for the algorithm are simple and involve a single computation of the forward and back-projection per iteration. Empirically, we have observed that the above algorithm results in a monotonic sequence of decreasing cost function values.

C. Implementation Details

Since the proposed MBIR cost function is non-convex and setting T is not straightforward, we initialize the algorithm by running the method (Fig. 4) N times for K iterations with the T set to a large number and progressively decrease T each time so that it rejects a certain fraction of the measurements (For results in this paper, $N = 5$ and $K = 10$). At the final stage we fix T, initialize f from the previous stage and run the algorithm till the stopping criteria is met or the maximum number of iterations is attained. We initialize the values of f to 0 at the start of the algorithm. The gradient of the data-fidelity term is implemented using the ASTRA tool-box's multi-GPU operators [33] in which the forward and back-projection are not matched [34] and are based on simple models [37] to accelerate the computation on GPUs at the expense of accuracy. Despite of this, we have not observed any divergent behavior or appearance of significant artifacts, though we believe the use of matched projectors could help

function $[\hat{f}] \leftarrow$ RECONSTRUCT(g, f^{init})
  %**Inputs**: Measurements g, Initial reconstruction f^{init}
  %**Outputs**: Reconstruction $\hat{f}$
  $t^{(0)} = 1, f^{(0)} = h^{(0)} = f^{\text{init}}$
  Compute gradient step size L
  for $k = 1$ to K **do** ▷ K - maximum iterations
    $e^{(k)} = y - Af^{(k)}$ ▷ Initialize error vector
    Update $W^{(k)}$ based on $e^{(k)}$ and threshold T (6)
    Compute gradient: $-A^t W^{(k)} e^{(k)} + \nabla s(f^{(k)})$
    Compute $f^{(k+1)}, h^{(k+1)}, t^{(k+1)}$ using equations (8)
    if stopping criteria is met **then**
      break
    end if
  end for
  $\hat{f} \leftarrow f^{(k+1)}$
end function

Fig. 4. Overall MBIR algorithm for laminography.

attain a better reconstruction. The gradient of the prior is implemented to be parallel so each thread operates on a subset of voxels.

IV. Results

We compare reconstructions from three algorithms : the modified filtered back projection (FBP) [10], SIRT [13] and the MBIR method. For the FBP and SIRT we pre-process the raw data using a median filter using the TomoPy package [38] to filter out the gamma-hits. The maximum number of iterations for the MBIR method was set to 200 and the algorithm was terminated if the relative change in the average value of the reconstruction was less than 0.1%. The value of p is set to 1.2 for the MBIR reconstructions. All reconstructions were carried out using a server with 22 Intel Xeon-Phi cores, 512 Gb of RAM and 2 P100 Nvidia GPUs each with 24 Gb of memory.

A. Simulated Data

We constructed a high-resolution phantom to represent an additively manufactured part with pores (see Fig. 5 (a)) and generated laminography projections of size 128×256 pixels at 400 views between $0^\circ - 360^\circ$ with the laminography angle set to 70°. We simulated gamma-hits at approximately 6 random locations in 40% of the views and simulated Poisson statistics for the noise. Fig. 5 (b) shows cross-sections of the reconstruction from the FBP method. Notice that the reconstructions are noisy, with poor resolution for the pore features and artifacts in the $x - z$ and $y - z$ planes due to the missing cones of information. The SIRT reconstruction (Fig. 5 (c)) is sharper than the FBP reconstruction but still has residual noise and the artifacts due to the missing cones of information. In contrast, the proposed MBIR method significantly suppresses the missing cone artifacts and produces a quantitatively accurate, less noisy and a visually better resolution for the reconstruction. To emphasize the importance of outlier modeling we also compare the proposed MBIR algorithm with a similar method based on a quadratic $l(g; f)$ and demonstrate (Fig. 6) that the modeling for the outliers (gamma-hits) dramatically improves the quality of reconstruction without any pre-processing applied to the data. We note that, similar artifacts were seen for the FBP and SIRT algorithm, but leave these images out in the interest of brevity.

B. Experimental Data

The experimental data set is obtained from an additively manufactured metal part made of a Chromium-Cobalt alloy at the manufacturing demonstration facility (MDF) at Oak Ridge National Lab (ORNL). Because of its unique shape and composition, neutron laminography is an important technique to make the measurements and characterize defects such as pores in the 3D printed sample. Measurements were made at the High-Flux Isotopte Reactor (HFIR) at the CG-1D beamline and consisted of 1094 views between $0 - 360^\circ$ using a 2048×2048 pixel detector with the laminography angle set to 70°. We use a 700×1600 window of pixels (Fig. 1) to reconstruct a $700 \times 1600 \times 1600$ voxel volume. Fig. 7 demonstrates how the MBIR algorithm can produce a high quality reconstruction (high visual resolution for similar noise levels) from this noisy-data set even from the raw un-filtered measurements compared to the FBP and SIRT algorithm. Similarly to the simulated data, Fig. 8 illustrates that merely using a MBIR based on quadratic $l(g; f)$ can result in streaks in various directions and these can be misclassified as pores if the analysis is done on individual $x - y$ cross sections of the reconstructed volume. Hence, the robust modeling provides a useful way to handle gamma-hits as a part of the reconstruction.

V. Conclusion

In this paper, we presented a robust MBIR algorithm for neutron laminography. The algorithm is based on optimizing a cost-function that accounts for the noise characteristics, the presence of gamma-hits and provides the flexibility to choose from a family of regularization functions. We presented an optimization algorithm based on constructing a majorization function and using it to update the voxels using a first-order algorithm that enables us to perform the updates rapidly using massively parallel architectures. We applied our algorithm to simulated and experimental data to illustrate that our method is superior to traditional direct inversion and algebraic iterative algorithms in obtaining high-quality reconstructions from the raw measurements.

VI. Acknowledgements

The HFIR is supported by the Office of Basic Energy Sciences of the U.S. Department of Energy. Research at MDF was sponsored by the U.S. Department of Energy, Office of Energy Efficiency and Renewable Energy, Advanced Manufacturing Office, under contract DE-AC05-00OR22725 with UT-Battelle, LLC. This work was partially funded by Oak Ridge National Lab via the Laboratory Directed Research and Development program. This work was also partly supported by the DOE Advanced Scientific Computing Research, through the ACUMEN project.

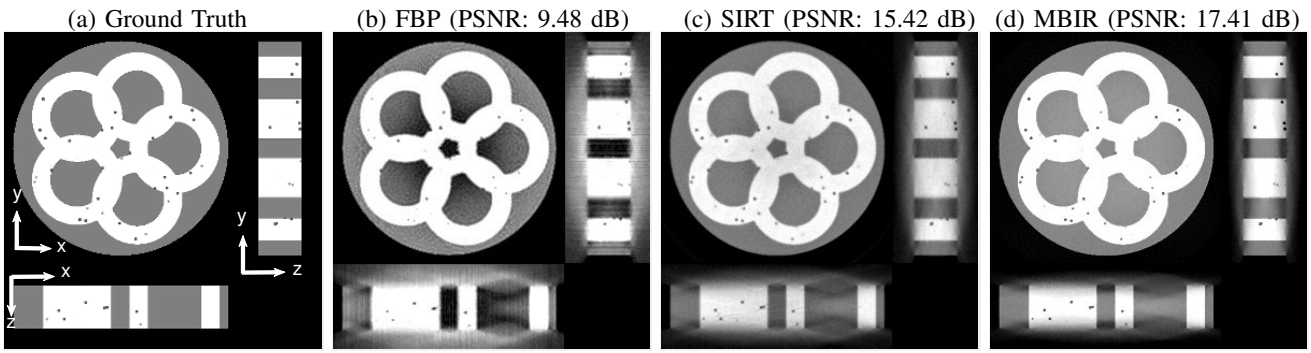

Fig. 5. Cross-sections from the 3D reconstruction using FBP, SIRT and the proposed MBIR from a simulated data set representing an additively manufactured part with pores. Notice that the FBP reconstruction has artifacts due to the sampling geometry (missing cones) and some ringing due the filter used. The SIRT reconstruction is more accurate than FBP, but still has a worse noise v/s resolution performance than the proposed MBIR. The MBIR also significantly suppresses the artifacts due to missing data compared to both FBP and SIRT. Furthermore, unlike the FBP and SIRT methods, the MBIR method was applied without any pre-processing using median filters.

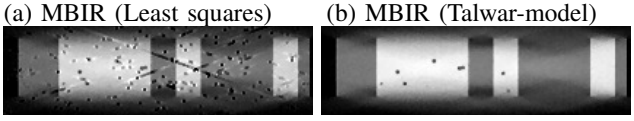

Fig. 6. Illustration of the artifacts in a $x-z$ cross section (same as in Fig. 5) that occur when the gamma hits on the detector are not accounted for by the pre-processing even when using a sophisticated model-based inversion algorithm with a weighted-least squares data-fit penalty. However, using the proposed algorithm (b), outliers can be detected and rejected as a part of the reconstruction without pre-filtering the data.

REFERENCES

[1] S. Gondrom, J. Zhou, M. Maisl, H. Reiter, M. Krning, and W. Arnold, "X-ray computed laminography: an approach of computed tomography for applications with limited access," *Nuclear Engineering and Design*, vol. 190, no. 1, pp. 141 – 147, 1999.

[2] L. T. Niklason, B. T. Christian, L. E. Niklason, D. B. Kopans, D. E. Castleberry, B. H. Opsahl-Ong, C. E. Landberg, P. J. Slanetz, A. A. Giardino, R. Moore, D. Albagli, M. C. DeJule, P. F. Fitzgerald, D. F. Fobare, B. W. Giambattista, R. F. Kwasnick, J. Liu, S. J. Lubowski, G. E. Possin, J. F. Richotte, C. Y. Wei, and R. F. Wirth, "Digital tomosynthesis in breast imaging." *Radiology*, vol. 205, no. 2, pp. 399–406, 1997.

[3] M. De Villiers, "Limited angle tomography," Ph.D. dissertation, University of Cape Town, 2004.

[4] M. Holler, M. Guizar-Sicairos, E. H. R. Tsai, R. Dinapoli, E. Müller, O. Bunk, J. Raabe, and G. Aeppli, "High-resolution non-destructive three-dimensional imaging of integrated circuits," *Nature*, vol. 543, no. 7645, pp. 402–406, Mar 2017, Letter.

[5] F. Salvemini, F. Grazzi, N. Kardjilov, I. Manke, F. Civita, and M. Zoppi, "Neutron computed laminography on ancient metal artefacts," *Analytic Methods*, vol. 7, 11 2014.

[6] F. Xu, L. Helfen, A. J. Moffat, G. Johnson, I. Sinclair, and T. Baumbach, "Synchrotron radiation computed laminography for polymer composite failure studies," *Journal of Synchrotron Radiation*, vol. 17, no. 2, pp. 222–226, Mar 2010.

[7] N. S. O'Brien, R. P. Boardman, I. Sinclair, and T. Blumensath, "Recent Advances in X-ray Cone-beam Computed Laminography," *J Xray Sci Technol*, vol. 24, no. 5, pp. 691–707, Oct 2016.

[8] L. Helfen, A. Myagotin, P. Mikulk, P. Pernot, A. Voropaev, M. Elyyan, M. D. Michiel, J. Baruchel, and T. Baumbach, "On the implementation of computed laminography using synchrotron radiation," *Review of Scientific Instruments*, vol. 82, no. 6, p. 063702, 2011.

[9] L. Helfen, F. Xu, B. Schillinger, E. Calzada, I. Zanette, T. Weitkamp, and T. Baumbach, "Neutron laminography - a novel approach to three-dimensional imaging of flat objects with neutrons," *Nuclear Instruments and Methods in Physics Research Section A: Accelerators, Spectrometers, Detectors and Associated Equipment*, vol. 651, no. 1, pp. 135 – 139, 2011, proceeding of the Ninth World Conference on Neutron radiography.

[10] A. Myagotin, A. Voropaev, L. Helfen, D. Hnschke, and T. Baumbach, "Efficient volume reconstruction for parallel-beam computed laminography by filtered backprojection on multi-core clusters," *IEEE Transactions on Image Processing*, vol. 22, no. 12, pp. 5348–5361, Dec 2013.

[11] A. Voropaev, A. Myagotin, L. Helfen, and T. Baumbach, "Direct fourier inversion reconstruction algorithm for computed laminography," *IEEE Transactions on Image Processing*, vol. 25, no. 5, pp. 2368–2378, May 2016.

[12] L. Helfen, F. Xu, H. Suhonen, L. Urbanelli, P. Cloetens, and T. Baumbach, "Nano-laminography for three-dimensional high-resolution imaging of flat specimens," *Journal of Instrumentation*, vol. 8, no. 05, p. C05006, 2013.

[13] A. C. Kak and M. Slaney, *Principles of Computerized Tomographic Imaging*. Philadephia, PA: Society for Industrial and Applied Mathematics, 2001.

[14] C. A. Bouman, *Model Based Image Processing*, 2013. [Online]. Available: https://engineering.purdue.edu/~bouman/publications/pdf/MBIP-book.pdf

[15] S. Venkatakrishnan, L. Drummy, M. Jackson, M. De Graef, J. Simmons, and C. Bouman, "A model based iterative reconstruction algorithm for high angle annular dark field - scanning transmission electron microscope (HAADF-STEM) tomography," *IEEE Trans. on Image Processing*, vol. 22, no. 11, Nov. 2013.

[16] ——, "Model based iterative reconstruction for bright-field electron tomography," *IEEE Trans. on Computational Imaging*, vol. 1, no. 1, pp. 1–15, March 2015.

[17] K. A. Mohan, S. V. Venkatakrishnan, L. F. Drummy, J. Simmons, D. Y. Parkinson, and C. A. Bouman, "Model-based iterative reconstruction for synchrotron X-ray tomography," Proc. of IEEE ICASSP 2014.

[18] K. Mohan, S. Venkatakrishnan, J. Gibbs, E. Gulsoy, X. Xiao, M. De Graef, P. Voorhees, and C. Bouman, "TIMBIR: A method for time-space reconstruction from interlaced views," *Computational Imaging, IEEE Transactions on*, vol. 1, no. 2, pp. 96–111, June 2015.

[19] Z. Yu, J. Thibault, C. Bouman, K. Sauer, and J. Hsieh, "Fast model-based X-ray CT reconstruction using spatially nonhomogeneous ICD optimization," *IEEE Trans. on Image Processing*, vol. 20, no. 1, pp. 161 –175, Jan. 2011.

[20] K. J. Batenburg, W. J. Palenstijn, and J. Sijbers, "3D imaging of semiconductor components by discrete laminography," *AIP Conference Proceedings*, vol. 1601, no. 1, pp. 168–179, 2014.

[21] S. Abbas, M. Park, and S. Cho, "Fast and low-dose computed laminography using compressive sensing based technique," *AIP Conference Proceedings*, vol. 1650, no. 1, pp. 586–590, 2015.

[22] S. V. Venkatakrishnan, L. F. Drummy, M. De Graef, J. P. Simmons, and C. A. Bouman, "Model based iterative reconstruction for bright field electron tomography," *Proc. SPIE 8657, Computational Imaging XI, 86570A (February 14, 2013)*, pp. 86 570A–86 570A–12, 2013.

[23] J. Zheng, S. Saquib, K. Sauer, and C. Bouman, "Parallelizable Bayesian tomography algorithms with rapid, guaranteed convergence," *Image Processing, IEEE Transactions on*, vol. 9, no. 10, pp. 1745–1759, 2000.

[24] H. Erdogan and J. Fessler, "Monotonic algorithms for transmission tomography," *Medical Imaging, IEEE Transactions on*, vol. 18, no. 9, pp. 801–814, 1999.

[25] D. Kim and J. A. Fessler, "An optimized first-order method for image

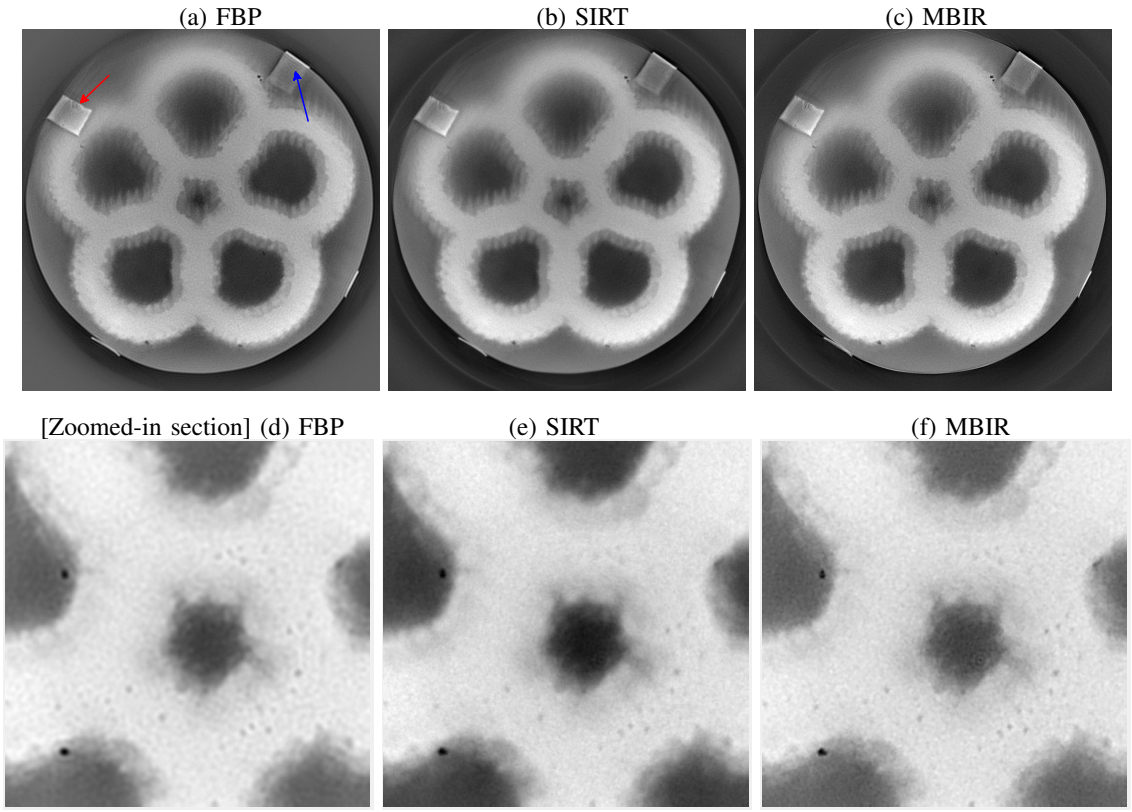

Fig. 7. $x-y$ cross-sections from the 3D reconstruction using FBP, SIRT and the proposed MBIR from a data set of an additively manufactured part. Notice that the for a given background noise level, the MBIR produces higher resolution images (visually) compared to FBP and SIRT (For example - regions indicated by red arrow in (a) and the zoomed-in images of (d), (e) and (f)). Furthermore, there are ringing artifacts in the FBP (blue-arrow) reconstruction due to the filtering of the projections that are suppressed by SIRT and the proposed MBIR method.

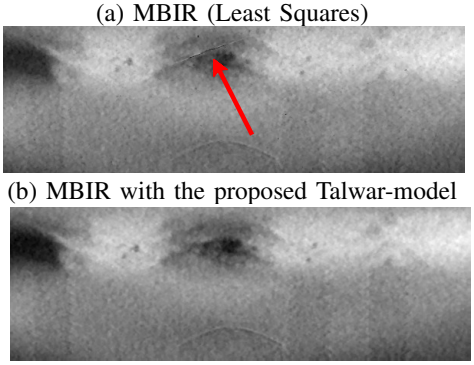

Fig. 8. Illustration of artifacts (indicated with a red arrow in (a)) in a $y-z$ cross section that occur when the gamma hits on the detector are not accounted for by the pre-processing even when using a MBIR algorithm based on a weighted-least squares data-fit penalty. However, using the proposed algorithm (b), outliers can be detected and rejected as a part of the reconstruction without pre-filtering the data.

restoration," in *2015 IEEE International Conference on Image Processing (ICIP)*, Sept 2015, pp. 3675–3679.

[26] S. V. Venkatakrishnan, M. Farmand, Y. S. Yu, H. Majidi, K. van Benthem, S. Marchesini, D. A. Shapiro, and A. Hexemer, "Robust X-ray phase ptycho-tomography," *IEEE Signal Processing Letters*, vol. 23, no. 7, pp. 944–948, July 2016.

[27] P. J. Huber and E. M. Ronchetti, *Robust Statistics*. Wiley, 2009.

[28] M. J. Hinich and P. P. Talwar, "A simple method for robust regression," *Journal of the American Statistical Association*, vol. 70, no. 349, pp. 113–119, 1975.

[29] M. Kubinova and J. G. Nagy, "Robust regression for mixed Poisson-Gaussian model," *arXiv:1611.07774*, 2016.

[30] K. Sauer and C. Bouman, "Bayesian Estimation of Transmission Tomograms Using Segmentation Based Optimization," *IEEE Trans. on Nuclear Science*, vol. 39, pp. 1144–1152, 1992.

[31] W. Palenstijn, K. Batenburg, and J. Sijbers, "Performance improvements for iterative electron tomography reconstruction using graphics processing units (GPUs)," *Journal of Structural Biology*, vol. 176, no. 2, pp. 250 – 253, 2011.

[32] W. van Aarle, W. J. Palenstijn, J. D. Beenhouwer, T. Altantzis, S. Bals, K. J. Batenburg, and J. Sijbers, "The ASTRA toolbox: A platform for advanced algorithm development in electron tomography," *Ultramicroscopy*, vol. 157, no. Supplement C, pp. 35 – 47, 2015.

[33] W. van Aarle, W. J. Palenstijn, J. Cant, E. Janssens, F. Bleichrodt, A. Dabravolski, J. D. Beenhouwer, K. J. Batenburg, and J. Sijbers, "Fast and flexible X-ray tomography using the ASTRA toolbox," *Opt. Express*, vol. 24, no. 22, pp. 25 129–25 147, Oct 2016.

[34] F. Bleichrodt, T. van Leeuwen, W. J. Palenstijn, W. van Aarle, J. Sijbers, and K. J. Batenburg, "Easy implementation of advanced tomography algorithms using the ASTRA toolbox with Spot operators," *Numerical Algorithms*, vol. 71, no. 3, pp. 673–697, Mar 2016.

[35] J.-B. Thibault, K. Sauer, C. Bouman, and J. Hsieh, "A three-dimensional statistical approach to improved image quality for multislice helical CT," *Med. Phys.*, vol. 34, pp. 4526–4544, 2007.

[36] S. Abbas, M. Park, J. Min, H. K. Kim, and S. Cho, "Sparse-view computed laminography with a spherical sinusoidal scan for nondestructive testing," *Opt. Express*, vol. 22, no. 15, pp. 17 745–17 755, Jul 2014.

[37] P. M. Joseph, "An improved algorithm for reprojecting rays through pixel images," *IEEE Transactions on Medical Imaging*, vol. 1, no. 3, pp. 192–196, Nov 1982.

[38] D. Gürsoy, F. De Carlo, X. Xiao, and C. Jacobsen, "TomoPy: a framework for the analysis of synchrotron tomographic data," *Journal of Synchrotron Radiation*, vol. 21, no. 5, pp. 1188–1193, Sep 2014.